NANO LETTERS

Letter

pubs.acs.org/NanoLett

Self-Assembly: A Facile Way of Forming Ultrathin, High-Performance Graphene Oxide Membranes for Water Purification

Weiwei L. Xu,[†] Chao Fang,[‡] Fanglei Zhou,[†] Zhuonan Song,[†] Qiuli Liu,[†] Rui Qiao,[‡] and Miao Yu*[,†]

[†]Department of Chemical Engineering and Catalysis for Renewable Fuels Center, University of South Carolina, Columbia, South Carolina 29208, United States

[‡]Department of Mechanical Engineering, Virginia Tech, Blacksburg, Virginia 24061, United States

Supporting Information

ABSTRACT: Single-layer graphene oxide (SLGO) is emerging as a new-generation membrane material for high-flux, high-selectivity water purification, owing to its favorable two-dimensional morphology that allows facile fabrication of ultrathin membranes with subnanometer interlayer channels. However, reliable and precise molecular sieving performance still necessarily depends on thick graphene oxide (GO) deposition that usually leads to low water flux. This trade-off between selectivity and flux significantly impedes the development of ultrathin GO membranes. In this work, we demonstrate that the selectivity/flux trade-off can be broken by self-assembly of SLGO via simple deposition rate control. We find GO membranes, prepared by slow deposition of SLGO flakes, exhibit considerably improved salt rejection, while counterintuitively having 2.5−4 times higher water flux than that of membranes prepared by fast deposition. This finding has extensive implications of designing/tuning interlayer nanostructure of ultrathin GO membranes by simply controlling SLGO deposition rate and thus may greatly facilitate their development for high flux, high selectivity water purification.

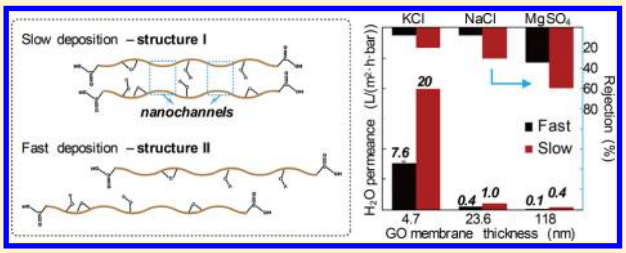

KEYWORDS: *Graphene oxide, membrane, self-assembly, interlayer nanostructure, water purification*

Recently, single-layer graphene oxide (SLGO) has attracted increasing attention as a new membrane material due to its atomically thin thickness, two-dimensional (2D) structure, and high chemical stability.[1−6] Owing to the large number of oxygen-containing functionalization groups, SLGO can be easily dispersed in water. Consequently, solution-based coating processes, such as vacuum filtration, have been applied to fabricate graphene oxide (GO) membranes with lamellar structure and subnanometer interlayer nanochannels.[7,8] Previous studies have illustrated that the 2D nanochannels between adjacent SLGO flakes can provide pathways for size-dependent molecular sieving and frictionless water permeation.[7,9−11] Encouraged by these exciting experimental results, many following studies have focused on exploring the water purification potential of GO membranes with lamellar structure.[12−20] While numerous attempts have been made to fabricate ultrathin (<100 nm) SLGO-based membranes for water treatment recently,[12,13,20] only relatively thick membranes exhibit reliable and precise sieving performance so far.[7,9,10,16]

Fundamentally, the permeation characteristics of a GO membrane with lamellar structure are expected to be mainly governed by the interlayer nanostructure formed between neighboring SLGOs. Different from graphene, SLGO features abundant oxygen-containing surface functional groups. Therefore, the interlayer nanostructure of SLGO-based membranes depends on how the surface functional groups of adjacent SLGO layers are arranged. So far, no study has been conducted to understand the interlayer nanostructure and its influence on water purification performance. To develop ultrathin membranes with both high permeation rate and excellent selectivity, it is essential to understand process-structure-performance relationship of SLGO-based membranes, that is, how membrane fabrication conditions control the membrane interlayer nanostructures and how interlayer nanostructures in turn determine the permeation characteristics.

In this study, we explore the process-structure-performance relationship of GO membranes prepared by vacuum filtration. Here, we purposely deposited SLGO at a fast rate and at a rate ∼12 times slower to control the interlayer nanostructure of the resulting membranes. We find, while maintaining the same SLGO loading per unit area, the slowly deposited GO membranes show greatly enhanced water permeation rate. We propose that at slow deposition rate SLGO flakes better self-assemble to approach the thermodynamically favored interlayer structure with functionalized patches on neighboring GO layers facing each other and pristine graphene patches on adjacent GO layers forming fast water transport channels (type I structure, Figure 1). At fast deposition rate, relatively random packing of SLGOs is locked into less favorable interlayer structures with significant mismatches between functionalized and pristine patches on neighboring GO layers (type II structure, Figure 1), leading to drastically retarded water

Received: January 11, 2017
Revised: March 20, 2017
Published: April 7, 2017

ACS Publications © 2017 American Chemical Society

DOI: 10.1021/acs.nanolett.7b00148
Nano Lett. 2017, 17, 2928−2933

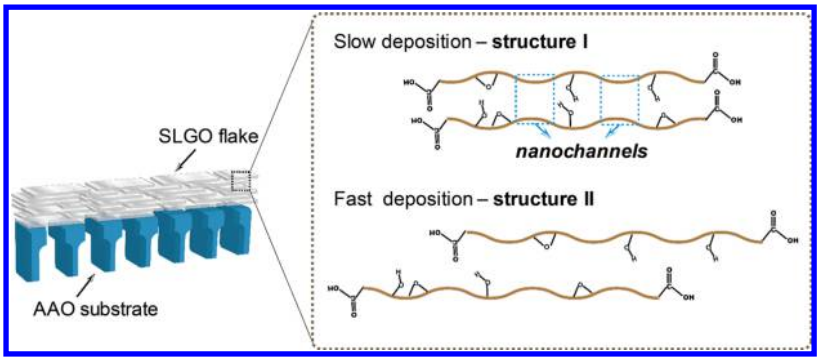

Figure 1. Proposed conceptual interlayer nanostructures of GO membranes prepared by slow and fast deposition rates. When prepared at slow deposition rate, oxygen-containing groups on adjacent SLGO flakes prefer to self-assemble with each other to form thermodynamically favored interlayer structure. In contrast, at fast deposition rate oxygen-containing groups may arrange in a more random fashion.

permeation. The different molecular details of these interlayer structures and their effect on water transport were corroborated by X-ray diffraction (XRD), organic vapor permeation, atomic force microscopy (AFM), and molecular dynamics (MD) simulations. Moreover, GO membrane as thin as 4.7 nm and with the favorable interlayer nanostructure exhibits considerably improved salt rejection. For the first time, this study clarifies the process-structure-performance of GO membranes, and the insight gained here can be utilized to guide new designs of ultrathin GO membranes for high-flux, high selectivity water purification.

GO was prepared by Hummers method.[21] After washing, sonication, and centrifugation, the as-synthesized GO show single-layer features with an average thickness of ~0.8 nm and a lateral size of ~500 nm (Figure 2a). The Raman spectrum

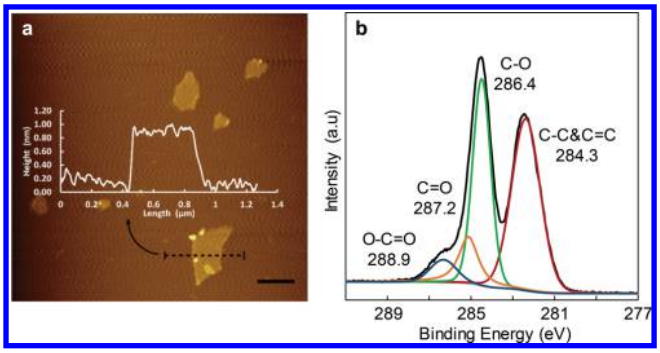

Figure 2. Characterization of single layer graphene oxide (SLGO). (a) AFM image of SLGO deposited on a mica substrate; inset shows the height profile of a SLGO flake (scale bar: 500 nm). (b) XPS C_1s spectrum of SLGO.

(Figure S1) exhibits a G peak at ~1590 cm^{-1} and a D peak at ~1350 cm^{-1}, assigned to the graphitized structure and local defects/disorders, respectively;[22,23] the low I_D/I_G ratio (1.39) suggests high order is still maintained in the graphitized structure of the synthesized GO.[24] Various oxygen-containing groups on SLGO are observed on the Fourier transform infrared (FTIR) spectrum (Figure S2). X-ray photoelectron spectroscopy (XPS) was also conducted to explore the chemical environment of carbon atoms in SLGO (Figure 2b), which indicates that ~49% of the carbon is nonoxidized, 41% is C—O bonded, and 10% attributes to C═O and COOH bonding. GO membranes were deposited on commercial anodized aluminum oxide (AAO) substrates (~20 nm pore size in the top layer) with an effective area of 10.5 cm^2 through a simple vacuum-filtration process (Figure S3a). Thickness of GO membranes was controlled by the amount of SLGO in the suspension (= liquid volume × SLGO concentration in suspension), and the actual SLGO concentration in suspension was measured by a total organic carbon (TOC) analyzer. The membrane thickness with GO loading of 184.4 mg/m^2 was determined from the cross-sectional scanning electron microscopy (SEM) image (Figure S3b), which is 118 ± 5.2 nm. Thickness of membranes with lower SLGO loadings was extrapolated by assuming it changes linearly with deposition amount.

In an attempt to fabricate the proposed two interlayer nanostructures (Figure 1), GO membranes with the same thickness/SLGO loading were prepared by dispersing the same amount of SLGO in 25 and 250 mL DI water, respectively, to allow fast and slow deposition by vacuum filtration. For instance, to prepare a 118 nm thick GO membrane, it took ~5 min to filter a 25 mL suspension with 0.19 mg of SLGO; for a 250 mL suspension with the same SLGO amount, ~1.5 h was needed to complete the filtration process. Accordingly, the average fast and slow deposition rates of the 118 nm thick GO membrane are calculated as 0.37 and 0.02 nm/s, respectively. The deposition rates of three different GO membrane thicknesses by the slow and fast deposition processes are summarized in Table S1. Thus, fabricated membranes are denoted as slow- and fast-deposited GO membranes in the following. Cross-sectional FESEM images of representative fast- and slow-deposited membranes were shown in Figure S4, demonstrating good lamellar structure of GO membranes prepared within our GO deposition rate range.

To explore the possible structure difference between slow- and fast-deposited GO membranes, XRD was first performed to measure the average interlayer spacing (*d*-spacing). XRD analysis was conducted for a 118 nm thick GO membrane to obtain better signal (Figure 3a). The XRD pattern shows that the (001) peak of the fast-deposited GO membrane locates at 10.46°, whereas that of slow-deposited GO membrane is at 10.72°. This suggests that the average interlayer spacing is slightly narrowed from 8.4 to 8.2 Å, when SLGO flakes were slowly deposited on AAO surface. As shown in Figure S5, similar trend could be found on thermally reduced GO membranes. After reduction, the interlayer spacing of the fast-deposited GO membrane shrinks to 3.9 Å, whereas the slow-deposited membrane shows even tighter packing with an interlayer distance of ~3.5 Å. These XRD results suggest that different deposition rates might bring about structural change in GO membranes, and slow deposition leads to narrower

DOI: 10.1021/acs.nanolett.7b00148
Nano Lett. 2017, 17, 2928−2933

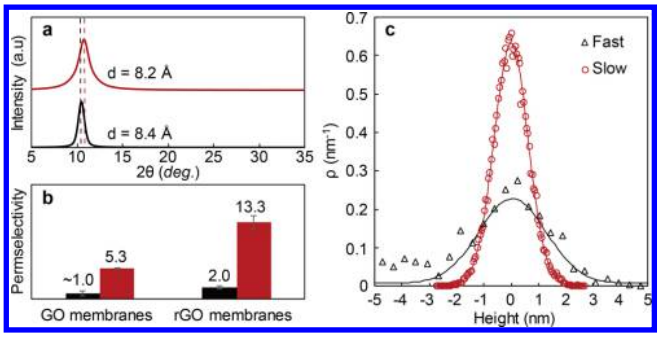

Figure 3. Characterization of fast- and slow-deposited GO membranes. (a) XRD patterns of 118 nm thick GO membranes prepared by fast (black) and slow (red) deposition rates. (b) Permselectivity for *n*-hexane over 2,2-dimethylbutane (DMB) of fast- (black) and slow-deposited (red), 118 nm thick GO and corresponding rGO membranes which prepared by mild thermal reduction. (c) Height distributions for the top layer of two overlapped SLGO flakes prepared at fast (black) and slow (red) deposition rate; the AFM scan was conducted for the samples exposed to 100% water relative humidity. The solid line is the Gaussian fit of height distribution. To clarify the top layer roughness difference between overlapped SLGO flakes prepared at slow and fast deposition conditions, the mean of the Gaussian fit was set as zero and the height distribution curve was shifted accordingly as well.

interlayer nanochannels. XPS measurements of reduced GO membranes were conducted to further clarify the structural difference between slow- and fast-deposited GO membranes and its influence on mild thermal reduction (Tables S5 and S6). After reduction, GO membrane prepared at slow deposition rate exhibits higher C/O ratio (1.61) than the fast-deposited one (1.49), implying that the narrower interlayer nanostructure of slow-deposited GO membrane might facilitate the dehydration of GO in the thermal reduction process.

Vapor permeation measurements (Figure S6 for the experimental setup) for two probe molecules, hexane (kinetic diameter: 0.43 nm) and 2,2-dimethylbutane (DMB; kinetic diameter: 0.62 nm), were also employed to investigate the effective size of nanochannels between SLGO flakes of slow- and fast-deposited GO membranes. Because these two isomers have different vapor pressure (17.6 kPa for hexane and 36.88 kPa for DMB) and thus different driving force for permeation, permeance (= permeation rate/(membrane area × pressure drop) = flux/pressure drop) was used to study the permeation rate difference and selectivity of membranes. The vapor permeation results (Figure 3b) exhibit that hexane transported ~5 times faster than DMB in the slow-deposited GO membrane, whereas the corresponding fast-deposited GO membrane shows no obvious difference. Compared with fast-deposited membrane, although the permeation of both hexane

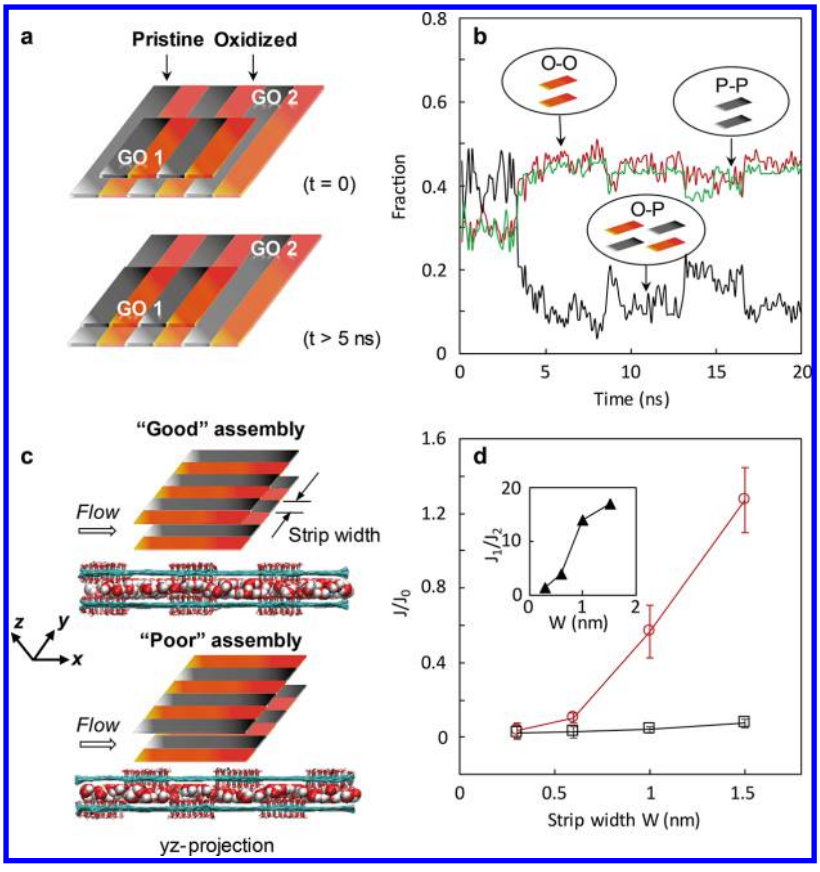

Figure 4. Self-assembly of SLGO in water and water transport through interlayer nanochannels. (a) A sketch of the two heterogeneous SLGOs used in self-assembly simulations. The oxidized and pristine strips of the two SLGOs are offset by ~0.5 nm at the beginning of self-assembly. (b) Evolution of the three types of subdomains of the SLGO during self-assembly. Inset sketches the subdomain types: O−O (an oxidized surface of one GO faces an oxidized surface of the other GO), P−P (a pristine surface of one GO faces a pristine surface of the other GO), and O−P (an oxidized surface of one GO faces a pristine surface of the other GO). (c) Sketches of the systems for studying water transport through two SLGO flakes in good and poor assembly configurations. (d) Normalized mass flux from "good" (red) and "poor" (black) assembly configurations with different strip sizes. The inset shows the ratio of water flux for good and poor assembly configurations as a function of strip size.

DOI: 10.1021/acs.nanolett.7b00148
Nano Lett. 2017, 17, 2928−2933

and DMB is retarded in the slow-deposited membrane, DMB permeates ∼8 time slower, whereas hexane only ∼1.3 times (Table S3). This suggests that the higher hexane/DMB selectivity of slow-deposited GO membrane might be attributed to the narrower *d*-spacing/average nanochannel size, which drags down the transport of larger DMB more than that of hexane. The influence of deposition rate on organic vapor permeation becomes even more notable for the reduced GO membranes. After reduction, the permselectivity (ratio of the permeances) of hexane over DMB of the slow-deposited membrane increases to 13, while the fast-deposited one has a selectivity of only ∼2. These vapor permeation results indicate GO membrane prepared at slow deposition rate possesses smaller effective size of the interlayer nanochannels, which further supports the XRD results. Because hexane and DMB are expected to interact more favorably with hydrophobic domains in GO membranes and thus their main transport pathway is expected to be the hydrophobic nanochannels, the nanochannel size explored is probably corresponding the hydrophobic domains.

Understanding water adsorption on and between SLGO flakes and the response of interlayer nanostructures upon water adsorption may further help reveal the difference between interlayer nanostructures formed by slow and fast deposition of SLGO. Water adsorption isotherm on SLGO indicates that water molecules may preferentially adsorb on hydrophilic sites and thus do not form a continuous water phase between GO flakes (Figure S10 and its discussion). Considering different hydrophilic sites/oxygen-containing groups distribution between SLGO flakes, type I and type II structures are expected to respond differently to water adsorption. AFM was applied to investigate surface roughness change, when two SLGO flakes were stacked together by fast and slow deposition processes and then exposed to different humidity (Figure S11 for experimental details). As water molecules are shown to adsorb preferentially on the oxidized sites of GO flakes, AFM topological scanning on 100%-water-saturated overlapped SLGO flakes prepared at different deposition rates could provide evidence for our deposition-rate-correlated interlayer nanostructures. For the overlapped SLGO flakes deposited at slow evaporation rate of water, well-assembled hydrophilic groups (type I structure) are expected to result in fewer exposed water accumulation sites between the GO flakes. In contrast, as overlapped SLGO flakes were deposited at a fast evaporation rate, more hydrophilic sites are expected to be exposed to water (type II structure), and consequently make the top layer surface rougher. The height distribution diagram indicates that under dry condition both fast- and slow-deposited SLGO bilayers have similar top layer surface roughness (Figure S11d). While under 100% relative humidity, the Gaussian fit for the height distribution of the fast-deposited SLGO bilayer presents a full width at half-maximum (fwhm) of 2.9 nm, whereas slow-deposited GO bilayer has a fwhm of only 1.5 nm, as shown in Figure 3c, demonstrating that the surface of the fast-deposited GO bilayer is about twice as rough as the slow-deposited one. This is consistent with our assumption and supports the conclusion that fast deposition rate leads to type II nanostructure, while the type I nanostructure results at a slow deposition rate.

To ascertain that the type I nanostructure is indeed thermodynamically more favorable than the type II nanostructure, we performed molecular dynamics (MD) simulations to study the self-assembly of SLGO flakes in water. Prior experiments and simulations revealed that the surfaces of GOs are heterogeneous: oxygen-containing surface groups tend to cluster together to form oxidized patches with size of 1−2 nm, thus leaving many pristine areas free of functionalization groups.[25−29] Here, without losing generality we simulated the self-assembly of two SLGO flakes both featuring 1 nm wide strips of oxidized and pristine surfaces (Figure 4a). The self-assembly of SLGO in water can lead to different interlayer structures depending on the relative arrangement of oxidized and pristine surfaces in the neighboring GOs. The interlayer structure formed by these two SLGO flakes typically exhibits three types of subdomains (inset in Figure 4b): an oxidized surface facing another oxidized surface (O−O), a pristine surface facing another pristine surface (P−P), and an oxidized surface facing a pristine surface (O−P). The O−O and P−P subdomains correspond to the type I structure shown in Figure 1, while the O−P subdomain corresponds to the type II structure. At the beginning of the self-assembly process, the oxidized strips of the two SLGOs are offset by ∼0.5 nm. Hence the interlayer nanostructure is dominated by O−P subdomains (∼50%). As shown in Figure 4b, as the self-assembly proceeds, the fraction of O−P subdomains decreases, whereas that of the O−O and P−P subdomains increases. At $t > 5$ ns, the interlayer structure approaches equilibrium with the fractions of O−O and P−P subdomains both approaching 40%. Overall, self-assembly of SLGOs in liquid water favors the formation of type I interlayer structure over type II interlayer structure.

The interlayer structure between SLGO flakes can potentially influence the transport of water molecules through GO membranes. We examine its effect using MD simulations. Given the complexity and heterogeneity of the interlayer structure in practical GO membranes are difficult to be fully accounted for in simulations, here we consider only two limiting cases (Figure 4c): the "good" assembly that contains only O−O and P−P subdomains and the "poor" assembly that contains only O−P subdomains. For SLGO flakes featuring alternating strips of pristine and oxidized surfaces, these two interlayer structures are idealistic representations of the type I and II structures illustrated in Figure 1, and they correspond to the most and least thermodynamically favorable states of packed SLGO. Because the size of pristine and oxidized patches in real GO membranes shows a statistical distribution, we varied the width of pristine and oxidized strips in both "good" assembly and "poor" assembly from 0.3 to 1.5 nm in different simulations. In these simulations, the spacing between SLGO flakes was taken as 0.69 nm, the equilibrium spacing between SLGOs found in the above self-assembly simulations. Adopting a constant spacing is in line with the experimental observation which, for GO membranes prepared by different methods, the difference in the interlayer spacing is on the order of subangstroms;[30,31] we also verify that using a different spacing does not qualitatively change the water transport behavior (Figure S13b). Figure 4d compares the water flux through the nanochannels between the SLGO flakes with "good" and "poor" assemblies. For a strip width of 1.5 nm, the mass flux of water in the "good" assembly case is slightly higher than that predicted by using the classical Poiseuille flow equation, but the flux in the "poor" assembly case is about 10 times lower than the Poiseuille flow prediction. As shown in the inset of Figure 4d, the water flux in the two different structures becomes similar as the strip width reduces but remains significant for a strip width of 1.0 nm. The water flux is higher in the "good" assembly case because the hydrophobic nanochannels in the

DOI: 10.1021/acs.nanolett.7b00148
Nano Lett. 2017, 17, 2928−2933

P−P subdomains provide more effective transport pathways for water molecules than the nanochannels in the O−O and O−P subdomains. In the latter subdomains, water molecules form extensive hydrogen bonds with the OH groups on the surface of SLGO, which impedes the transport of water.[30,32] Note that water flux in the "good" assembly case does not greatly exceed that predicted by classical theory assuming no-slip boundary condition at GO−water interfaces. This is consistent with the recent findings that the slip of water monolayers confined between the hydrophobic patches in GO membranes is greatly suppressed by the slow transport of the water molecules confined between oxidized patches (termed "side-pinning" in some studies).[33] Nevertheless, it is clear that water permeance is faster through type I interlayer structure than through type II interlayer structure.

Motivated by the above predictions that interlayer structure of GO membranes significantly affects the water transport through the membranes, we next experimentally measured the flux of pure water through fast- and slow-deposited GO membranes. We find that the slow-deposited GO membranes have much higher water permeance (pressure normalized water flux) than the fast-deposited membranes. As shown in Figure 5a, the slow-deposited 4.7- and 23.6 nm GO membranes show

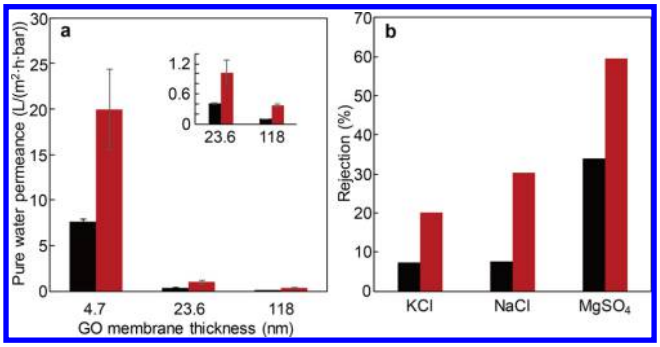

Figure 5. (a) Water permeation through GO membranes prepared by fast (black) and slow-deposition (red) rates; inset shows the water permeance of two thicker membranes at smaller scale of *y*-axis. (b) Salt rejection of 4.7 nm thick GO membrane prepared at fast/slow deposition rate.

~2.5 times higher steady state water permeance than that of the fast-deposited ones. As the thickness increasing to 118 nm (inset, Figure 5a), the water permeance of the slow-deposited membrane is around 4 times higher than that of the fast-deposited GO membrane. Because slow-deposited GO membranes are expected to feature more type I interlayer structure than the fast-deposited membranes, these observations corroborate the MD predictions that water transport is faster through GO membranes with type I interlayer structure. The difference of water permeance in slow- and fast-deposited GO membranes is not as significant as that revealed in the MD simulations because the oxidized regions on SLGO surfaces in real GO membranes is unlikely to be well-aligned as modeled in the MD simulations.

To demonstrate superior nanofiltration performance of slow-deposited GO membranes, long-term salt rejection tests for KCl, NaCl and $MgSO_4$ were conducted on 4.7 nm GO membranes due to its high water permeance, and the rejection results for various salts reported in Figure 5b represent steady state results, meaning no measurable changes within last 2 h. Figure 5b shows that the slow-deposited GO membrane with favorable nanostructure after self-assembly has 1.8−4 times higher salt rejection than that of the fast-deposited GO membrane. As far as we know, this is the thinnest GO membrane with comparable salt rejection as that of much thicker GO membranes.[12,13] The slow-deposited, 4.7 nm GO membrane maintains its higher salt rejection at higher salt concentration, as shown in Figure S12; as concentration increases to 50 and 100 mM, slow-deposited GO membrane still exhibits at least ~2 times higher NaCl rejection than that of the fast-deposited GO membrane. Thus, the ion exclusion results clearly illustrate that a membrane with type I structure has better size-dependent sieving properties besides its greatly enhanced water flux.

In summary, we demonstrate that interlayer nanostructures between SLGO flakes can be "tuned" between type I structure and type II structure, as shown in Figure 1, by simply controlling SLGO flake deposition rate in solution phase deposition process. Structure characterization and MD simulations confirm that type I structure is more thermodynamically favored structure and facilitates fast water permeation. Experimental results show that compared with type II structure, narrower hydrophobic nanochannels in type I structure lead to 2.5−4 times faster water permeation rate and 1.8−4 times higher salt rejection. We believe this finding helps break the current trade-off between water flux and precise sieving performance of GO membranes and may eventually lead to novel design of ultrathin GO-based membranes for high flux and high selectivity water purification.

■ ASSOCIATED CONTENT

Supporting Information

The Supporting Information is available free of charge on the ACS Publications website at DOI: 10.1021/acs.nanolett.7b00148.

Synthesis and basic characterization of graphene oxide, fabrication and characterization of GO membranes, water flux measurement, organic vapor permeation measurement, water adsorption isotherm of GO, AFM topology scan on overlapped GO double-layer under different humidity, MD simulation, and salt reject experiments details (PDF)

The self-assembly of two SLGOs during a 20 ns long production run (MPG)

■ AUTHOR INFORMATION

Corresponding Author

*E-mail: yumiao@cec.sc.edu.

ORCID

Weiwei L. Xu: 0000-0001-7671-4753

Rui Qiao: 0000-0001-5219-5530

Notes

The authors declare no competing financial interest.

■ ACKNOWLEDGMENTS

We gratefully acknowledge the support by National Science Foundation (NSF) Career Award under Grant No. 1451887.

■ REFERENCES

(1) Geim, A. K.; Novoselov, K. S. *Nat. Mater.* **2007**, *6*, 183−191.
(2) Geim, A. K. *Science* **2009**, *324*, 1530−1534.
(3) Dreyer, D. R.; Park, S.; Bielawski, C. W.; Ruoff, R. S. *Chem. Soc. Rev.* **2010**, *39*, 228−240.

DOI: 10.1021/acs.nanolett.7b00148
Nano Lett. 2017, 17, 2928−2933

(4) Huang, H. B.; Ying, Y. L.; Peng, X. S. *J. Mater. Chem. A* **2014**, *2*, 13772−13782.
(5) Surwade, S. P.; Smirnov, S. N.; Vlassiouk, I. V.; Unocic, R. R.; Veith, G. M.; Dai, S.; Mahurin, S. M. *Nat. Nanotechnol.* **2015**, *10*, 459−464.
(6) Fathizadeh, M.; Xu, W. L.; Zhou, F.; Yoon, Y.; Yu, M. *Adv. Mater. Interfaces* **2017**, *4*, 1600918.
(7) Nair, R. R.; Wu, H. A.; Jayaram, P. N.; Grigorieva, I. V.; Geim, A. K. *Science* **2012**, *335*, 442−444.
(8) Rezania, B.; Severin, N.; Talyzin, A. V.; Rabe, J. P. *Nano Lett.* **2014**, *14*, 3993−3998.
(9) Sun, P. Z.; Zhu, M.; Wang, K. L.; Zhong, M. L.; Wei, J. Q.; Wu, D. H.; Xu, Z. P.; Zhu, H. W. *ACS Nano* **2013**, *7*, 428−437.
(10) Joshi, R. K.; Carbone, P.; Wang, F. C.; Kravets, V. G.; Su, Y.; Grigorieva, I. V.; Wu, H. A.; Geim, A. K.; Nair, R. R. *Science* **2014**, *343*, 752−754.
(11) Sun, P. Z.; Liu, H.; Wang, K. L.; Zhong, M. L.; Wu, D. H.; Zhu, H. W. *Chem. Commun.* **2015**, *51*, 3251−3254.
(12) Han, Y.; Xu, Z.; Gao, C. *Adv. Funct. Mater.* **2013**, *23*, 3693−3700.
(13) Hu, M.; Mi, B. X. *Environ. Sci. Technol.* **2013**, *47*, 3715−3723.
(14) Huang, H. B.; Mao, Y. Y.; Ying, Y. L.; Liu, Y.; Sun, L. W.; Peng, X. S. *Chem. Commun.* **2013**, *49*, 5963−5965.
(15) Li, H.; Huang, Y.; Mao, Y. T.; Xu, W. W. L.; Ploehn, H. J.; Yu, M. *Chem. Commun.* **2014**, *50*, 9849−9851.
(16) Sun, P. Z.; Zheng, F.; Zhu, M.; Song, Z. G.; Wang, K. L.; Zhong, M. L.; Wu, D. H.; Little, R. B.; Xu, Z. P.; Zhu, H. W. *ACS Nano* **2014**, *8*, 850−859.
(17) Zhang, Y.; Zhang, S.; Chung, T. S. *Environ. Sci. Technol.* **2015**, *49*, 10235−10242.
(18) Liu, H. Y.; Wang, H. T.; Zhang, X. W. *Adv. Mater.* **2015**, *27*, 249−254.
(19) Chong, J. Y.; Aba, N. F. D.; Wang, B.; Mattevi, C.; Li, K. *Sci. Rep.* **2015**, *5*, 15799.
(20) Akbari, A.; Sheath, P.; Martin, S. T.; Shinde, D. B.; Shaibani, M.; Banerjee, P. C.; Tkacz, R.; Bhattacharyya, D.; Majumder, M. *Nat. Commun.* **2016**, *7*, 10891.
(21) Marcano, D. C.; Kosynkin, D. V.; Berlin, J. M.; Sinitskii, A.; Sun, Z. Z.; Slesarev, A.; Alemany, L. B.; Lu, W.; Tour, J. M. *ACS Nano* **2010**, *4*, 4806−4814.
(22) Ferrari, A. C.; Robertson, J. *Phys. Rev. B: Condens. Matter Mater. Phys.* **2000**, *61*, 14095−14107.
(23) Graf, D.; Molitor, F.; Ensslin, K.; Stampfer, C.; Jungen, A.; Hierold, C.; Wirtz, L. *Nano Lett.* **2007**, *7*, 238−242.
(24) Cancado, L. G.; Jorio, A.; Ferreira, E. H. M.; Stavale, F.; Achete, C. A.; Capaz, R. B.; Moutinho, M. V. O.; Lombardo, A.; Kulmala, T. S.; Ferrari, A. C. *Nano Lett.* **2011**, *11*, 3190−3196.
(25) Wilson, N. R.; Pandey, P. A.; Beanland, R.; Young, R. J.; Kinloch, I. A.; Gong, L.; Liu, Z.; Suenaga, K.; Rourke, J. P.; York, S. J.; Sloan, J. *ACS Nano* **2009**, *3*, 2547−2556.
(26) Pacilé, D.; Meyer, J. C.; Fraile Rodríguez, A.; Papagno, M.; Gómez-Navarro, C.; Sundaram, R. S.; Burghard, M.; Kern, K.; Carbone, C.; Kaiser, U. *Carbon* **2011**, *49*, 966−972.
(27) Zhou, S.; Bongiorno, A. *Sci. Rep.* **2013**, *3*, 2484.
(28) Kumar, P. V.; Bardhan, N. M.; Tongay, S.; Wu, J.; Belcher, A. M.; Grossman, J. C. *Nat. Chem.* **2013**, *6*, 151−158.
(29) Erickson, K.; Erni, R.; Lee, Z.; Alem, N.; Gannett, W.; Zettl, A. *Adv. Mater.* **2010**, *22*, 4467−4472.
(30) Devanathan, R.; Chase-Woods, D.; Shin, Y.; Gotthold, D. W. *Sci. Rep.* **2016**, *6*, 29484.
(31) Talyzin, A. V.; Hausmaninger, T.; You, S. J.; Szabo, T. *Nanoscale* **2014**, *6*, 272−281.
(32) Wei, N.; Peng, X.; Xu, Z. *ACS Appl. Mater. Interfaces* **2014**, *6*, 5877−5883.
(33) Nair, R. R.; Wu, H. A.; Jayaram, P. N.; Grigorieva, I. V.; Geim, A. K. *Science* **2012**, *335*, 442−444.

DOI: 10.1021/acs.nanolett.7b00148
Nano Lett. 2017, 17, 2928−2933